POLITECNICO DI TORINO
Repository ISTITUZIONALE

Direct flux vector control of IPM motor drives in the maximum torque per voltage speed range

Original
Direct flux vector control of IPM motor drives in the maximum torque per voltage speed range / Pellegrino, G.-.M.L., Armando, E.G., Guglielmi, P.. - In: IEEE TRANSACTIONS ON INDUSTRIAL ELECTRONICS. - ISSN 0278-0046. - STAMPA. - 59:10(2012), pp. 3780-3788. [10.1109/TIE.2011.2178212]

Availability:
This version is available at: 11583/2460421 since:

Publisher:
IEEE

Published
DOI:10.1109/TIE.2011.2178212

Terms of use:

This article is made available under terms and conditions as specified in the corresponding bibliographic description in the repository

Publisher copyright
IEEE postprint/Author's Accepted Manuscript

©2012 IEEE. Personal use of this material is permitted. Permission from IEEE must be obtained for all other uses, in any current or future media, including reprinting/republishing this material for advertising or promotional purposes, creating new collecting works, for resale or lists, or reuse of any copyrighted component of this work in other works.

(Article begins on next page)

19 November 2026

An Adaptive Sampling Process for Automated Multivariate Macromodeling Based on Hamiltonian-Based Passivity Metrics

Elisa Fevola, Alessandro Zanco, Stefano Grivet-Talocia, Tommaso Bradde, Marco De Stefano
Dept. Electronics and Telecommunications, Politecnico di Torino, Torino, Italy
{elisa.fevola, alessandro.zanco, stefano.grivet, tommaso.bradde, marco.destefano}@polito.it

***Abstract*—This paper introduces a fully automated greedy algorithm for the construction of parameterized behavioral models of electromagnetic structures, targeting at the same time uniform model stability and passivity. The proposed algorithm is able to determine a small set of parameter configurations for which an external solver provides on the fly the sampled scattering parameters of the structure over a predetermined frequency band. These samples are subjected to a multivariate rational/polynomial fitting process, which iteratively leads to a parameterized descriptor realization of the model. The main novel contribution in this work is the adoption of a model-based approach for the adaptive augmentation of an initially small set of frequency responses, each corresponding to a randomly-selected parameter configuration. In particular, the locations of the in-band passivity violations of intermediate macromodels constructed at each iteration are used as a proxy for the model-data error in those regions where input data are not available. This physics-based consistency check, which is enabled by recent developments in multivariate passivity characterization based on Skew-Hamiltonian-Hamiltonian (SHH) spectra, is combined with standard space exploration metrics to obtain a small-size and automatically-determined distribution of points in the parameter space, leading to the construction of an accurate macromodel with a very limited number of external field solver runs. The embedded passivity check and enforcement process guarantees that either the final model is passive throughout the parameter space, or the residual violations, if present, are negligible for practical purposes. Several examples validate the proposed approach for up to three concurrent parameters.**

I. Introduction

Most Computer-Aided Design (CAD) flows of linear electrical, electronic and electromagnetic structures depend on the availability of the frequency responses of the device, structure or system under investigation. These are most often obtained through full-wave electromagnetic simulations, which may be very costly in terms of computational resources and especially runtime. It is thus very desirable to complete the full design cycle, including optimization, centering and what-if analyses, while minimizing the required number of such full-wave simulations.

Using surrogate, reduced-order, or behavioral models is a well-established practice in this scenario [1]–[3]. Surrogate models may be available in various forms: here we focus on linear finite-dimensional state-space or descriptor forms [4]–[6], which are the standard representation for lumped circuit equivalents. A surrogate model of a well-defined structure can be trained or identified from a sampled frequency response computed from a field solver [7]–[10]. With proper identification tools, it can be guaranteed that the model responses match the original samples to a prescribed accuracy level, thus enabling usage of the model in any subsequent numerical simulation in time or frequency domain. This avoids repeating costly full-wave simulations of the same structure under different working or termination conditions.

This work focuses on multivariate surrogate models [11]–[19], whose responses depend on frequency and on a set of additional parameters, which could represent either design variables for which an optimization is desired, or uncertain variables that are not under control. In the latter case, the design process should guarantee good performance under any combination of such uncertainties within their prescribed range of variation. Whatever be the nature of these parameters, a multivariate surrogate model needs to be identified or trained from a possibly large number of true scattering response samples in the frequency and parameter space. The denser is this grid of raw samples, the higher will be the confidence level that the model responses represent accurately the underlying system throughout the parameter space and the frequency band of interest. This is in contrast to the practical requirement of limiting the number of full-wave simulations for reducing computing cost and runtime.

This paper provides an adaptive sampling algorithm for the automatic selection of parameter combinations, for which a frequency sweep of an external field solver is performed. The main objective of the algorithm is the minimization of such parameter configurations, so that the number of field solutions is also reduced. As in most standard adaptive sampling schemes [20]–[23], the proposed algorithm starts with an initially small set of points in the parameter space. An iterative process is then started, which automatically determines which are the regions of the parameter space that need to be sampled more densely by adding points, in order to improve model quality. The final outcome that is expected is a multivariate macromodel in state-space (descriptor) form, which is guaranteed to be uniformly stable and passive throughout the parameter space in addition to being uniformly accurate.

Several previous works addressed the issue of multivariate macromodeling through adaptive sampling. In particular, there are two main approaches for driving adaptive sampling: data-driven approaches and model-driven approaches. In data-driven approaches [20], no intermediate models are used for

the selection of the parameter configurations to be computed by the field solver. Only the distribution of data (design space exploration) and the variation of the frequency responses (exploitation) are considered. These approaches work well when combined with macromodel parameterization schemes that are based on interpolation of univariate (non-parameterized) models. One of the main motivations for using a pure data-driven approach is to avoid the unnecessary costs of building intermediate models that will be discarded at the end of the adaptive sampling loop.

We propose in this work a complementary model-driven approach [22]–[24], based on the fundamental assumption that the field solver cost is much higher than the cost for extracting the macromodels. In addition to a space exploration criterion, which we preserve due to the obvious necessity of spanning the entire design space and thus avoiding to miss any areas in which the structure is not properly characterized, we use two model-based criteria. At any iteration we build a candidate multivariate model based on the current distribution of points. First, a standard criterion based on the model-data error at the available points is used to identify the regions where the model is less accurate, thus pointing to the locations where new points should be added in order to improve accuracy. The main novel contribution of this work is a second model-based criterion built on the multivariate passivity characterization of [25] and further developed in [26]–[28]. In fact, the model-data error can only be computed where data points are available, so that this metric has very limited predictive capabilities to infer the model quality in poorly sampled regions. Conversely, a multivariate passivity check of the model is able to automatically identify the boundaries of the regions where the model presents passivity violations, irrespective on the distribution of the available data points. The passivity violations provide a localization of the areas where the model is physically-inconsistent, which is exactly where its accuracy should be improved. New points are therefore added in these areas.

At the end of the proposed model-driven adaptive sampling loop, both model-data error and passivity violation extents are small at the available data points. Therefore, a final passivity enforcement is able to correct any residual passivity violations and leads to the desired parameterized model, with the guarantee that any residual passivity violations -if present- are negligible. We illustrate through various examples that the proposed scheme is able to construct such models using a very limited number of data samples, and for some cases significantly less data points than competing approaches.

This paper provides a complete theoretical framework for the method introduced in the preliminary work [29] and is organized as follows. Section II provides some background information on the adopted model structure and identification scheme, together with a summary of the main results of [25], [26] on Skew-Hamiltonian/Hamiltonian (SHH) pencil perturbation for passivity check and enforcement of multivariate models. Section III introduces the proposed adaptive sampling strategy, with a quantitative description of relevant metrics provided in Sec. IV. Numerical examples for up to three parameters are discussed in Sec. V.

II. Background

Throughout this work, vectors are typeset with boldface lowercase fonts, e.g., $\mathbf{x}$, and matrices with boldface uppercase fonts, e.g., $\mathbf{X}$. We denote the complex conjugate, the transpose, and the Hermitian transpose of a generic matrix as $\mathbf{X}^*$, $\mathbf{X}^\mathsf{T}$, and $\mathbf{X}^\mathsf{H}$, respectively.

A. Parameterized macromodeling from sampled responses

The main objective of this paper is the construction of a parameterized reduced-order P-port macromodel, whose response $\mathbf{H}(s;\boldsymbol{\vartheta}) \in \mathbb{C}^{P\times P}$ depends on frequency s and on a set of ρ external parameters collected in vector $\boldsymbol{\vartheta} = [\vartheta^1, ..., \vartheta^\rho]^\mathsf{T}$. The parameter vector spans a compact domain $\boldsymbol{\vartheta} \in \Theta \subset \mathbb{R}^\rho$, which without loss of generality will be assumed to be a ρ-dimensional normalized hypercube, with each component $\vartheta^\nu \in [0,1]$. Although the adopted notation allows for an arbitrary value of ρ, in this work we present results for up to $\rho = 3$ independent parameters. A discussion on the main limitations that hinder scalability to higher dimensions is deferred to Sec. IV-G.

The model is constructed from a set of frequency response data

$$\breve{\mathbf{H}}_{k,m} = \breve{\mathbf{H}}(\mathrm{j}\omega_k;\boldsymbol{\vartheta}_m), \quad k = 1,\dots,\bar{k},\ m = 1,\dots,\bar{m} \tag{1}$$

available, e.g., from a field solver. These data span a prescribed frequency range Ω and should adequately cover the parameter space Θ. The main purpose of this paper is to minimize the number $\bar{m}$ of parameter samples to be used for model construction, while guaranteeing a uniformly accurate, stable and passive model. We will consider in the following both data and models in scattering representation.

Among the several parameterized macromodeling schemes, we consider the approach based on the Parameterized Sanathanan-Koerner (PSK) iteration [11], [30], [31], which seeks a model with structure

$$\mathbf{H}(s;\boldsymbol{\vartheta}) = \frac{\mathbf{N}(s,\boldsymbol{\vartheta})}{\mathsf{D}(s,\boldsymbol{\vartheta})} = \frac{\sum_{n=0}^{\bar{n}}\sum_{\ell=1}^{\bar{\ell}} \mathbf{R}_{n,\ell}\,\xi_\ell(\boldsymbol{\vartheta})\,\varphi_n(s)}{\sum_{n=0}^{\bar{n}}\sum_{\ell=1}^{\bar{\ell}} r_{n,\ell}\,\xi_\ell(\boldsymbol{\vartheta})\,\varphi_n(s)} \tag{2}$$

where $\varphi_n(s)$ denotes the standard partial fraction basis associated to a set of initial "basis" poles q_n, e.g., $\varphi_0(s) = 1$ and $\varphi_n(s) = (s-q_n)^{-1}$ for $n > 0$, and where $\xi_\ell(\boldsymbol{\vartheta})$ denotes a set of multivariate basis functions, suitably ordered and indexed by a single global scalar index ℓ. Various choices for these basis functions have been successfully demonstrated, including partial fractions [13], orthogonal polynomials [28], piecewise linear or polynomial functions [11], [30], and trigonometric polynomials [12]. In this work we use order-$\bar{\ell}_\nu$ Chebychev polynomials for each independent parameter direction ϑ^ν, although this choice is not restrictive.

The model (2) is fully characterized by its numerator and denominator coefficients $\mathbf{R}_{n,\ell}$ and $r_{n,\ell}$, which are determined through the following iterative process

$$\min \left\| \frac{\mathbf{N}^\mu(\mathrm{j}2\pi f_k,\boldsymbol{\vartheta}_m) - \mathsf{D}^\mu(\mathrm{j}2\pi f_k,\boldsymbol{\vartheta}_m)\,\breve{\mathbf{H}}_{k,m}}{\mathsf{D}^{\mu-1}(\mathrm{j}2\pi f_k,\boldsymbol{\vartheta}_m)} \right\|_F^2 \tag{3}$$

which provides a relaxed linearized formulation of the model-data error minimization, and where the superscript $\mu =$

$1, 2, \ldots$ denotes iterations. At each iteration μ the estimates $\mathbf{R}_{n,\ell}^{\mu}$ and $r_{n,\ell}^{\mu}$ of the model coefficients are provided by a linear least squares solution of (3). Such coefficients stabilize at convergence.

The model is deemed acceptable if the model-data error is below a given threshold ε throughout the parameter space. Here we define the model error as the worst-case among all port responses of the frequency-domain RMS deviation

$$\mathcal{E}(\boldsymbol{\vartheta}_m) = \max_{i,j} \sqrt{\frac{1}{\bar{k}} \sum_{k=1}^{\bar{k}} \left| H_{ij}(\mathrm{j}\omega_k; \boldsymbol{\vartheta}_m) - (\breve{\mathbf{H}}_{k;m})_{ij} \right|^2}. \quad (4)$$

The model (2) is easily converted into a parameterized descriptor form

$$\mathbf{H}(s, \boldsymbol{\vartheta}) = \mathbf{C}(\boldsymbol{\vartheta}) \left(s\mathbf{E} - \mathbf{A}(\boldsymbol{\vartheta}) \right)^{-1} \mathbf{B} \quad (5)$$

with real realization matrices $\mathbf{E}, \mathbf{A} \in \mathbb{R}^{\bar{N} \times \bar{N}}$, $\mathbf{B} \in \mathbb{R}^{\bar{N} \times P}$ and $\mathbf{C} \in \mathbb{R}^{P \times \bar{N}}$, where

$$\mathbf{A}(\boldsymbol{\vartheta}) = \sum_{\ell=1}^{\bar{\ell}} \mathbf{A}_\ell \, \xi_\ell(\boldsymbol{\vartheta}), \quad \mathbf{C}(\boldsymbol{\vartheta}) = \sum_{\ell=1}^{\bar{\ell}} \mathbf{C}_\ell \, \xi_\ell(\boldsymbol{\vartheta}). \quad (6)$$

Details on the construction of the above descriptor realization are available in [11].

B. Hamiltonian-based passivity characterization

Most of the developments in this work are enabled by some recent results [26] on passivity characterization and enforcement in the present parameterized setting. We recall that a scattering model $\mathbf{H}(s, \boldsymbol{\vartheta})$ is *uniformly passive* $\forall \boldsymbol{\vartheta} \in \Theta$ if the following three *Uniform Bounded Realness* conditions [6], [32] hold:

a) $\mathbf{H}(s, \boldsymbol{\vartheta})$ regular for $\Re\{s\} > 0$ and $\forall \boldsymbol{\vartheta} \in \Theta$,
b) $\mathbf{H}^*(s, \boldsymbol{\vartheta}) = \mathbf{H}(s^*, \boldsymbol{\vartheta})$ $\forall s \in \mathbb{C}$ and $\forall \boldsymbol{\vartheta} \in \Theta$,
c) $\mathbb{I} - \mathbf{H}^{\mathsf{H}}(s, \boldsymbol{\vartheta}) \mathbf{H}(s, \boldsymbol{\vartheta}) \geq 0$ for $\Re\{s\} > 0$ and $\forall \boldsymbol{\vartheta} \in \Theta$.

The theory that is developed in [26], [27] shows that the Skew Hamiltonian-Hamiltonian (SHH) pencil $(\mathbf{M}_S(\boldsymbol{\vartheta}), \mathbf{K}_S)$ defined as

$$\mathbf{M}_S(\boldsymbol{\vartheta}) = \begin{bmatrix} \mathbf{A}(\boldsymbol{\vartheta}) & \mathbf{B}\mathbf{B}^{\mathsf{T}} \\ -\mathbf{C}^{\mathsf{T}}(\boldsymbol{\vartheta})\mathbf{C}(\boldsymbol{\vartheta}) & -\mathbf{A}^{\mathsf{T}}(\boldsymbol{\vartheta}) \end{bmatrix}$$
$$\mathbf{K}_S = \begin{bmatrix} \mathbf{E}^{\mathsf{T}} & \mathbf{0} \\ \mathbf{0} & \mathbf{E} \end{bmatrix} \quad (7)$$

plays a fundamental role in checking passivity, in particular condition c) above. In fact, assuming that the model is real-valued (condition b) and uniformly (asymptotically) stable (condition a), it can be shown that uniform (strict) passivity holds if and only if[1] the SHH pencil $(\mathbf{M}_S(\boldsymbol{\vartheta}), \mathbf{K}_S)$ has no purely imaginary eigenvalues $\forall \boldsymbol{\vartheta} \in \Theta$.

The passivity check algorithm presented in [26] proceeds as follows (we only summarize the main ideas here, see [26] for a full description).

1) The parameter space Θ is first subdivided into a regular grid of patches, induced by some initial coarse-level subdivision of each parameter range into equal subintervals (see Fig. 1a).

[1]additional technical conditions are required, which are however straightforward to verify and/or enforce, see [37]–[40] for details.

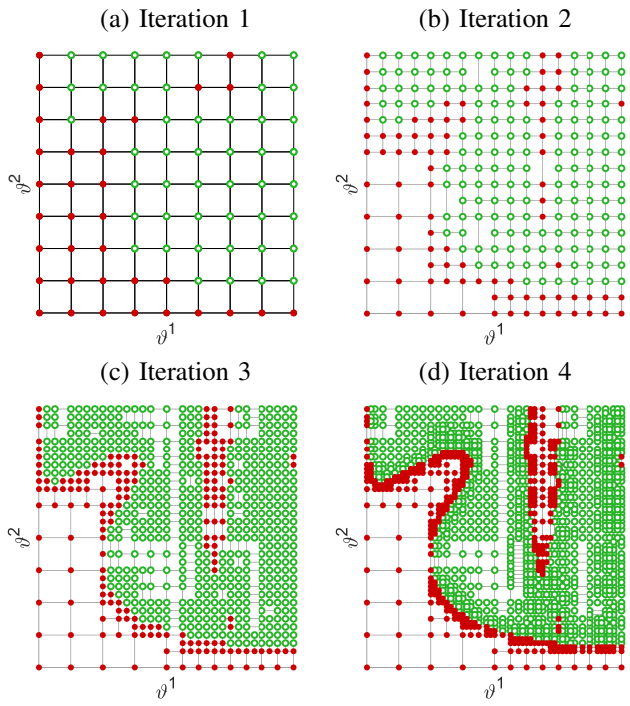


Fig. 1. Four successive iterations of the passivity verification algorithm presented in [26]. Empty green and filled red dots represent parameter configurations for which the model is passive or non-passive, respectively.

2) For each vertex $\hat{\boldsymbol{\vartheta}}_p$ of the above initial grid the SHH pencil $(\mathbf{M}_S(\hat{\boldsymbol{\vartheta}}_p), \mathbf{K}_S)$ is constructed, its eigenvalues are computed, and the vertex is flagged as "non-passive" or "passive" (red and green dots in Fig. 1, respectively) depending on whether imaginary eigenvalues are present or not.
3) The non-imaginary SHH eigenvalues at each passive vertex $\hat{\boldsymbol{\vartheta}}_p$ are subjected to a linear perturbation to predict their trajectories when $\boldsymbol{\vartheta} \approx \hat{\boldsymbol{\vartheta}}_p + \delta\boldsymbol{\vartheta}$ inside each patch. If these trajectories become too close to the imaginary axis (henceforth denoting a possible onset of a localized violation as $\boldsymbol{\vartheta}$ moves in the parameter space), then the patch is refined, new vertices are added as required by the refinement process, and their SHH eigenvalues are extracted.
4) Step 3 is repeated iteratively, until no refinements are necessary. Figures 1a–d depict the evolution of the adaptive grid, showing that the boundaries between passive (green) and non-passive (red) regions become more and more resolved through refinement iterations.
5) For each non-passive grid sample $\hat{\boldsymbol{\vartheta}}_p$, the corresponding largest singular value of the model response $\bar{\sigma}_p = \max \sigma(\mathbf{H}(\mathrm{j}\omega, \hat{\boldsymbol{\vartheta}}_p))$ is computed by an adaptive frequency sampling loop within each detected local violation band and stored. Since associated to a non-passive point, we have $\bar{\sigma}_p > 1$. Note that the grid samples in Fig. 1 represent regions with $\bar{\sigma}_p > 1$ (red dots) and $\bar{\sigma}_p < 1$ (green dots).

Figure 2 depicts the frequency-dependent singular value trajectories of a model at a non-passive sample point $\hat{\boldsymbol{\vartheta}}_p$, corresponding to one of the red dots in Fig. 1. The yellow dots

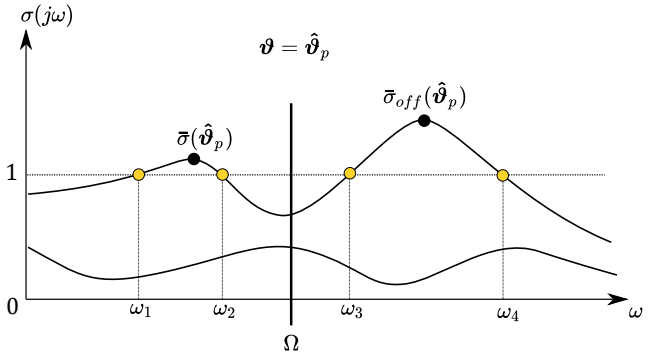


Fig. 2. Passivity characterization of a scattering macromodel instantiated at $\boldsymbol{\vartheta} = \hat{\boldsymbol{\vartheta}}_p$ in terms of local singular value maxima (see text).

correspond to the frequencies of the purely imaginary SHH eigenvalues, used to detect the passivity violation bands, in this case (ω_1, ω_2) localized within the modeling bandwidth, and (ω_3, ω_4) located out-band. The corresponding local maxima $\bar{\sigma}(\hat{\boldsymbol{\vartheta}}_p)$ and $\bar{\sigma}_{\text{off}}(\hat{\boldsymbol{\vartheta}}_p)$ correspond to the worst-case in-band and out-band passivity violations at $\hat{\boldsymbol{\vartheta}}_p$.

C. Checking uniform stability

The Hamiltonian check of Sec. II-B can be applied with minimal modifications also to check uniform stability of the model (condition a of Sec. II-B), which was assumed a priori in the above passivity check. It is shown in [28] that when the denominator $\mathsf{D}(s, \boldsymbol{\vartheta})$ of (2) is *Uniformly Positive Real*, then its zeros $p_n(\boldsymbol{\vartheta})$ (which are the parameter-dependent poles of the model) are guaranteed to have a negative real part. Therefore, uniform stability can be inferred from a uniform passivity (positive realness) check applied to the denominator only. The same algorithm of Sec. II-B can thus be applied, but using an appropriate SHH pencil $(\mathbf{M}_{\mathsf{D}}(\boldsymbol{\vartheta}), \mathbf{K}_{\mathsf{D}})$ suitable for Positive Real functions and applied to a state-space realization of the (scalar) denominator

$$\mathsf{D}(s, \boldsymbol{\vartheta}) = \mathbf{C}_{\mathsf{D}}(\boldsymbol{\vartheta}) \left[s\mathbf{I} - \mathbf{A}_{\mathsf{D}}\right]^{-1} \mathbf{B}_{\mathsf{D}} + D_{\mathsf{D}}(\boldsymbol{\vartheta}) \tag{8}$$

This pencil reads

$$\begin{aligned} \mathbf{M}_{\mathsf{D}}(\boldsymbol{\vartheta}) &= \begin{bmatrix} \mathbf{A}_{\mathsf{D}} & \mathbf{0} & \mathbf{B}_{\mathsf{D}} \\ \mathbf{0} & -\mathbf{A}_{\mathsf{D}}^{\mathsf{T}} & -\mathbf{C}_{\mathsf{D}}^{\mathsf{T}}(\boldsymbol{\vartheta}) \\ \mathbf{C}_{\mathsf{D}}(\boldsymbol{\vartheta}) & \mathbf{B}_{\mathsf{D}}^{\mathsf{T}} & 2D_{\mathsf{D}}(\boldsymbol{\vartheta}) \end{bmatrix}, \\ \mathbf{K}_{\mathsf{D}} &= \begin{bmatrix} \mathbf{I} & \mathbf{0} & \mathbf{0} \\ \mathbf{0} & \mathbf{I} & \mathbf{0} \\ \mathbf{0} & \mathbf{0} & \mathbf{0} \end{bmatrix} \end{aligned} \tag{9}$$

In summary, for a given parameterized macromodel in form (2), both uniform stability and uniform passivity checks lead to an adaptively sampled parameter space as in Fig. 1, where the boundaries between passive/non-passive and stable/unstable regions become more and more resolved as iterations progress. The availability of these checks suggests to exploit their *independent* and *model-driven* sample locations by embedding them as components of the overall adaptive sampling process that requests new points to the field solver, in order to improve model quality towards a uniformly accurate, stable and passive model, and in a fully automated way.

D. Enforcing uniform stability and passivity

Before introducing the proposed global adaptive sampling scheme, we recall how uniform model stability and passivity can be enforced if violations are detected. The following paragraphs summarize the results of [26]–[28], which the Reader is referred to for details.

Let us assume that some stability violations are detected at a set of adaptively-determined parameter samples $\widetilde{\boldsymbol{\vartheta}}_p$ from the stability check of Sec. II-C. These violations are removed by embedding a set of corresponding Positive Realness constraints applied to the the denominator $\mathsf{D}(s, \boldsymbol{\vartheta})$ in the PSK iteration (3). These constraints read

$$\Re\{\mathsf{D}(s, \widetilde{\boldsymbol{\vartheta}}_p)\} \geq \alpha, \tag{10}$$

where $\alpha > 0$ is a strictly positive constant used to enforce strict positive realness at each sample $\widetilde{\boldsymbol{\vartheta}}_p$. When expressed in terms of the model coefficients, (10) results in a simple linear inequality constraint, which combined with (3) leads to a linearly constrained linear least squares problem at each PSK iteration. The latter is easily solved using standard convex optimization methods [33]. Our implementation of the PSK iteration embeds the constraints (10) at each iteration. For all examples reported in the paper we set $\alpha = 1$. A different choice of α does not have any practical influence both on the passivity and the accuracy of the macromodel, resulting in just a renormalization of all numerator and denominator coefficients.

In case of passivity violations, the algorithm in [26], [27] can be used to determine the perturbation that is required for the model coefficients $\mathbf{R}_{n,\ell} \leftarrow \mathbf{R}_{n,\ell} + \Delta\mathbf{R}_{n,\ell}$ for removing the passivity violations and obtain a uniformly passive model.

III. Adaptive Algorithm for Point Selection

In most applications, the main bottleneck for extracting parameterized macromodels lies in computing the true responses of the underlying system required for model identification, due to the necessity of running costly full-wave electromagnetic simulations. It is highly desirable to obtain an accurate model from a minimum number of data samples. This can only be achieved by means of a suitable adaptive algorithm for point selection.

A generic adaptive sampling algorithm works in an iterative way. A starting set of $\bar{q}_0$ system responses corresponding to $\mathcal{Q}_0 = \{\boldsymbol{\vartheta}_1, \ldots, \boldsymbol{\vartheta}_{\bar{q}_0}\}$ are initially scattered on the parameter space, with each simulation point $\boldsymbol{\vartheta}_q = [\vartheta_q^1, ..., \vartheta_q^\rho]$ being associated to a specific combination of scalar values for the system parameters. At any subsequent iteration $i > 0$, a new set of points $\mathcal{P}_i$ is added to the already existing set, so the total set of data points, composed of $\bar{q}_i$ elements, becomes $\mathcal{Q}_i = \mathcal{Q}_{i-1} \cup \mathcal{P}_i$. The algorithm stops when the number of points is detected to be sufficient.

The new points $\mathcal{P}_i$ can be selected based on various strategies. For instance, the algorithm in [20] is based on the following two criteria:

- *exploration*, aimed at ensuring that data points are spread over the space uniformly, avoiding the presence of under-sampled regions;

- *exploitation*, aimed at detecting the regions where the raw data samples undergo fast variations, based on the assumption that large gradients in the data responses require a denser sampling rate.

These two criteria are the basis for corresponding normalized metrics, defined in [20], which are used to identify regions which need a further refinement. The main advantage of these two metrics, as advocated in [20], is their pure *data-driven* nature, which does not require the availability of a tentative model at any iteration.

With respect to [20], this work proposes a completely different strategy. Based on the assumption that the computational time required to generate a surrogate model is much less than the time required to compute new data samples (as typical in electromagnetic applications), we adopt here a mixed data- and model-driven approach. On one hand, we retain the data-driven *exploration* criterion, since it is important to scan the entire parameter space to avoid undersampling. On the other hand, and since the final objective is here to obtain an accurate surrogate model, we construct a tentative parameterized macromodel at each iteration, on which we define two additional criteria based on:

- *model vs data error*, based on the obvious consideration that more points need to be added in the regions where the model is not sufficiently accurate with respect to data, assuming that the lack of accuracy is due to some missing intersample information;
- *extent of passivity violations*, based on the assumption that the regions where an intermediate model is not passive correspond to regions where the model is physically-inconsistent. More points are then added in these regions to help reducing the extent of such violations at the next iteration.

Differently from [20], we drop the data-driven *exploitation* criterion. Indeed, an extensive campaign of numerical experiments demonstrated that the corresponding metric is ineffective towards improving model quality when the above model-driven criteria are adopted. The above criteria and the corresponding metrics that define our proposed adaptive sampling scheme are introduced in more detail in Sec. IV.

IV. Metrics and New Points Selection

Let us consider the situation at the i-th iteration of the adaptive sampling loop, with $\bar{q}_i$ available points $\boldsymbol{\vartheta}_q \in \mathcal{Q}_i$ obtained from the preceding iterations. As proposed in [20], we first subdivide the parameter space into a set of disjoint cells $C_{i;q}$, with each cell including only one sample $\boldsymbol{\vartheta}_q$, henceforth denoted as *center*. This is achieved through a Voronoi tessellation [34] based on the available seed points $\boldsymbol{\vartheta}_q$, see e.g. Fig. 5. We recall that, given a set of seed points $\boldsymbol{\vartheta}_q$, a Voronoi tessellation is a subdivision of space into regions based on distance from seeds. In particular, each region is associated to a seed, and it contains the portion of space closer to that seed than to any other. These regions are identified as Voronoi cells $C_{i;q}$.

Following [20] we rank the cells $C_{i;q}$ (equivalently, the seed points $\boldsymbol{\vartheta}_q$) through a global metric $\Lambda_{i;q}$, with higher values of $\Lambda_{i;q}$ denoting cells that require refinement through addition of samples. As discussed above, the proposed global metric includes three components, itemized below.

A. Exploration

The *exploration* metric, as originally proposed in [20], aims at placing new points in those regions of space which have not been explored yet, hence more likely to be undersampled. This metric is based on a pure geometric criterion, determined by the fraction of the parameter space occupied by the volume $|C_{i;q}|$ of each cell $C_{i;q}$. We define the exploration metric coherently with [20] as

$$\Lambda'_{i;q} = \frac{|C_{i;q}|}{|\Theta|}\,. \tag{11}$$

B. Model-data Error

At each iteration, we use the available data points $\boldsymbol{\vartheta}_q \in \mathcal{Q}_i$ to generate an intermediate macromodel $\mathbf{H}_i(s;\boldsymbol{\vartheta})$ using the PSK iteration reviewed in Sec. II-A. This model is obtained through an additional inner loop that estimates the model order by iteratively increasing the polynomial order ℓ_ν along each parameter direction, starting from the corresponding order at the previous adaptive sampling iteration, and up to a maximum order imposed by the constraint $\prod_\nu \ell_\nu < \kappa \bar{q}_i$, with $\kappa < 1/2$ so that overfitting is avoided. Order estimation is stopped when the desired accuracy is attained at all data points, or when the maximum order is reached.

The parameter-dependent accuracy of this model is then used to define a second metric as

$$\Lambda''_{i;q} = \frac{\mathcal{E}_i(\boldsymbol{\vartheta}_q)}{\sum_{q=1}^{\bar{q}_i} \mathcal{E}_i(\boldsymbol{\vartheta}_q)}. \tag{12}$$

where $\mathcal{E}_i(\boldsymbol{\vartheta}_q)$ is the model-data error as defined in (4) for the model $\mathbf{H}_i(s;\boldsymbol{\vartheta})$ at current iteration. If needed, the relative error or some more advanced frequency-weighted error metric can be used, depending on the application requirements. Note that $\Lambda''_{i;q}$ evaluates the model-data error at all the available sample points $\boldsymbol{\vartheta}_q \in \mathcal{Q}_i$, which are all used for model training.

The above model-based error metric is likely to reveal regions where model fitting is poor. Given the automated order estimation process that is implemented and applied at each iteration, which should guarantee that a nearly-optimal intermediate model $\mathbf{H}_i(s;\boldsymbol{\vartheta})$ is attained as allowed by the current set of samples, we argue that the main reason for a poor fitting in some parameter space areas is an insufficient characterization of the true system response in those areas. Therefore, cells $C_{i;q}$ associated with the largest values of $\Lambda''_{i;q}$ are good candidates for refinement.

C. Localization and extent of passivity violations

The above-described model-data error metric is not sufficient for the determination of the optimal set of new points to be added to the existing samples $\mathcal{Q}_i$ at each iteration. In fact, the model accuracy can only be assessed at the location of the existing data points $\boldsymbol{\vartheta}_q \in \mathcal{Q}_i$, without any predictive capability on the model quality in areas that are not yet

adequately sampled. This is why we introduce in this paper a new and completely independent passivity-based metric, which is able to detect the regions where the model is physically inconsistent. These regions are those characterized by local passivity violations.

Assuming that the underlying structure is passive, and that all raw data samples fulfill the passivity requirements, then a model passivity violation at a given point $\hat{\boldsymbol{\vartheta}}_p$ is a clear indirect indication of model inaccuracy at $\hat{\boldsymbol{\vartheta}}_p$. Moreover, the amount of such passivity violation can be effectively used as a proxy to quantify the lack of model accuracy at $\hat{\boldsymbol{\vartheta}}_p$. The key enabling factor that motivates using this metric is the predictive capability of the Hamiltonian-based passivity check (see Sec. II-B), which will detect the locations of passivity violations in the parameter space *irrespective* of the set of data samples used to construct the model, therefore providing an additional independent criterion for placement of new data samples.

Let us recall from Sec. II-B that a local passivity violation at frequency ω and parameter $\hat{\boldsymbol{\vartheta}}_p$ is revealed by the condition

$$\sigma_{\max}(\mathbf{H}(\mathrm{j}\omega, \hat{\boldsymbol{\vartheta}}_p)) > 1, \tag{13}$$

where $\sigma_{\max}$ denotes the maximum singular value of its matrix argument. Such violation can be located at a frequency ω that may be within the modeling bandwidth Ω or outside the modeling bandwidth. It is well-known that out-of-band passivity violations are almost inevitable in macromodels derived from a frequency-domain fitting process. However, such violations can be easily removed by appropriate passivity enforcement schemes, usually applied in a postprocessing phase. Here, we concentrate only on in-band violations, located at frequencies where the model accuracy is important. We have verified that position and extent of out-of-band violations are practically unrelated to in-band model accuracy and are therefore useless for driving an adaptive sampling process for in-band accuracy improvement. Moreover, the model accuracy cannot be controlled anyway outside the fitting band.

We characterize the (in-band) passivity of the parameterized macromodel at the i-th iteration, instantiated at $\hat{\boldsymbol{\vartheta}}_p$, as

$$\bar{\sigma}(\hat{\boldsymbol{\vartheta}}_p) = \max_{\omega \in \Omega} \sigma_{\max}(\mathbf{H}_i(\mathrm{j}\omega, \hat{\boldsymbol{\vartheta}}_p)). \tag{14}$$

The SHH adaptive sampling scheme of Sec. II-B is here used to determine the points $\hat{\boldsymbol{\vartheta}}_p$ in the parameter space for which the model has in-band local passivity violations, with $\bar{\sigma}(\hat{\boldsymbol{\vartheta}}_p) > 1$. This requires a small modification of the scheme as presented in [26], with the SHH purely imaginary eigenvalue search here restricted to $\omega \in \Omega$ instead of $\omega \in [0, +\infty)$. See also Fig. 2 for a graphical illustration.

As discussed in Sec. II-B, the SHH scheme returns a grid of adaptively-determined samples $\hat{\boldsymbol{\vartheta}}_p \in \mathcal{A}_i$ where the SHH eigenvalues are tested (see Fig. 1). This set of points is returned as two disjoint subsets

$$\mathcal{A}_i = \mathcal{B}_i \cup \mathcal{M}_i \tag{15}$$

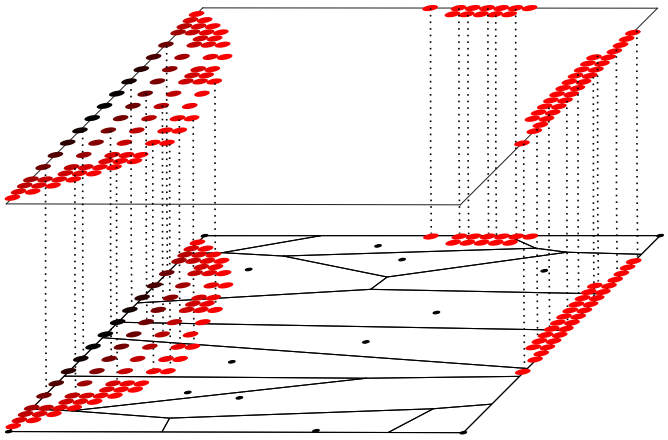


Fig. 3. Top plane: the points $\hat{\boldsymbol{\vartheta}}_p \in \Theta$ for which the model $\mathbf{H}(s, \hat{\boldsymbol{\vartheta}}_p)$ is not passive are colored according to the value of $\Delta_i(\hat{\boldsymbol{\vartheta}}_p)$ from 0 (red) to $\Delta_{i,\max}$ (black). Bottom plane: subdivision of the parameter space Θ into cells $C_{i;q}$ and associated centers $\boldsymbol{\vartheta}_q \in \mathcal{Q}_i$ at iteration i of the adaptive sampling loop.

where $\mathcal{B}_i$ and $\mathcal{M}_i$ include respectively all points $\hat{\boldsymbol{\vartheta}}_p$ at which the model is locally in-band passive and non-passive (green and red dots in Fig. 1, respectively). Denoting with

$$\Delta_{i,\max} = \max_{\hat{\boldsymbol{\vartheta}}_p \in \mathcal{A}_i} \bar{\sigma}(\hat{\boldsymbol{\vartheta}}_p) - 1 \tag{16}$$

the largest detected violation amount, we define the local in-band passivity violation as

$$\begin{cases} \Delta_i(\hat{\boldsymbol{\vartheta}}_p) = \bar{\sigma}(\hat{\boldsymbol{\vartheta}}_p) - 1, & \hat{\boldsymbol{\vartheta}}_p \in \mathcal{M}_i \\ \Delta_i(\hat{\boldsymbol{\vartheta}}_p) = 0, & \hat{\boldsymbol{\vartheta}}_p \in \mathcal{P}_i \end{cases} \tag{17}$$

in case at least one passivity violation is detected, so that $\Delta_{i,\max} > 0$. If the model is in-band passive, we have

$$\Delta_i(\hat{\boldsymbol{\vartheta}}_p) = 0 \qquad \forall \hat{\boldsymbol{\vartheta}}_p \in \mathcal{A}_i. \tag{18}$$

The top plane in Fig. 3 provides a perspective view of the grid points $\mathcal{M}_i$, depicted with shades of color according to the value of $\Delta_i(\hat{\boldsymbol{\vartheta}}_p)$ from 0 (red) to $\Delta_{i,\max}$ (black). Points in $\mathcal{B}_i$ are not drawn since not useful for our proposed passivity metric, to be defined next.

The passivity-based grid points $\mathcal{M}_i$ and the data-based cells $C_{i;q}$ at current iteration are superimposed, as depicted in Fig. 3. Each cell $C_{i;q}$ is thus enriched by the information provided by the local model passivity violations that it includes, if any. We define the proposed passivity metric for each cell $C_{i;q}$ as the worst-case passivity violation extent, computed among all points $\hat{\boldsymbol{\vartheta}}_p \in \mathcal{M}_i$ that belong also to $C_{i;q}$,

$$\Lambda'''_{i;q} = \max_{\hat{\boldsymbol{\vartheta}}_p \in C_{i;q} \cap \mathcal{M}_i} \Delta_i(\hat{\boldsymbol{\vartheta}}_p). \tag{19}$$

D. Global Metric

The three presented criteria are finally combined into an overall metric

$$\Lambda_{i;q} = w' \Lambda'_{i;q} + w'' \Lambda''_{i;q} + w''' \Lambda'''_{i;q} \tag{20}$$

where the weights $w', w'', w''' \geq 0$ can be used to tune the overall algorithm by giving more importance to the individual

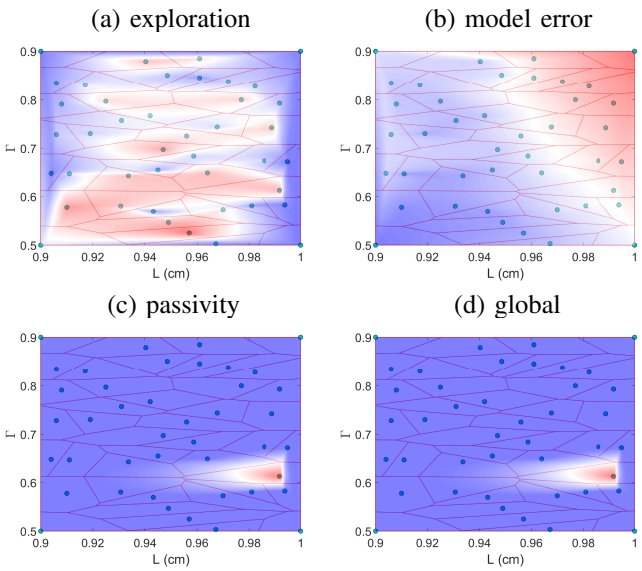


Fig. 4. The various panels depict the metrics used for cell ranking and refinement at each adaptive sampling iteration: (a) exploration metric $\Lambda'_{i;q}$ with range $[0.0134, 0.0385]$; (b) model-data error metric $\Lambda''_{i;q}$ with range $[0.0159, 0.0355]$; (c) passivity violation metric $\Lambda'''_{i;q}$ with range $[0, 0.07]$; and (d) global metric $\Lambda_{i;q}$. The four metrics are represented through independently normalized and linearly interpolated color shades ranging from the smallest (blue) to the largest (red) values. See text for additional details.

refinement criteria. This metric $\Lambda_{i;q}$ is used to rank the cells $C_{i;q}$, and only a fraction β of the cells with highest ranking will be subjected to refinement for the next pass of the adaptive sampling loop. Here we set $\beta = 1/3$, which we found as a good compromise between number of required iterations and computational cost at each iteration due to the evaluation of new data points.

Figure 4 provides a snapshot of the parameter space tessellation for one test case, where panels (a)-(c) report the three independent metric components $\Lambda'_{i;q}$, $\Lambda''_{i;q}$, $\Lambda'''_{i;q}$, respectively, and panel (d) depicts the global metric $\Lambda_{i;q}$. The figure shows that the three metrics provide independent ranking criteria, so that different choices of weighting coefficients result in significantly different cell rankings, hence different adaptive sampling patterns. The particular weighting scheme $w' = 1$, $w'' = 1$, $w''' = 10$ adopted in this example (and in all other examples in this paper) emphasizes the passivity-based metric, so that $\Lambda_{i;q}$ is dominated by $\Lambda'''_{i;q}$ in case passivity violations are present. If violations are not detected, the other two metrics become predominant.

E. Grid refinement

The adaptive sampling algorithm starts with an initial set of $\bar{q}_0$ points: $\rho 2^{\rho-1}$ samples are placed at the corners of the ρ-dimensional parameter space, while the remaining samples are randomly scattered in the space. At each refinement pass, the exact location of the new point inside each cell $C_{i;q}$ is here determined trying to maximize its distance both from the cell center $\boldsymbol{\vartheta}_q$ and from its closest neighbours $\mathcal{N}_i(\boldsymbol{\vartheta}_q)$. This choice is similar to [20], where however the cell center $\boldsymbol{\vartheta}_q$ was not considered. We found this difference to be important, since maximizing the distance only from neighboring points will tend to place the new point close to the center $\boldsymbol{\vartheta}_q$ of the considered cell, where a simulation point is in fact already present. Placing a new sample too close to an existing point is not useful in providing significantly new information to the already existing data set. We place the new point for each cell $C_{i;q}$ at the centroid of the largest triangle (simplex) obtained by connecting $\boldsymbol{\vartheta}_q$ to all cell vertices.

F. Stopping adaptive sampling iterations

The objective of presented algorithm is a uniformly accurate and passive macromodel throughout the parameter space. Therefore, we stop the adaptive sampling loop only when the model-data error (4) is below a prescribed acceptance threshold ε for all cells $C_{i;q}$. Additionally, and irrespective of the model accuracy, we continue iterations until all local in-band passivity violations are smaller than a prescribed threshold as $\Delta_{i,\max} < \varepsilon_p$, which we set for all examples to $\varepsilon_p = \varepsilon$. This additional constraint ensures that there are no points in the parameter space where the model is physically inconsistent, at least by an amount that cannot be reliably corrected in a postprocessing step.

The final model $\mathbf{H}(s, \boldsymbol{\vartheta})$ after stopping iterations is thus guaranteed to be uniformly accurate, but it is still not guaranteed to be uniformly passive. Some residual passivity violations may be present, either very small or out-band. Therefore, we launch one final passivity enforcement loop, which aims at removing all residual passivity violations while perturbing the macromodel coefficients. To this end, we use without modification the algorithm presented in [26].

A high level description of the proposed method is provided in Algorithm 1.

G. Limitations of the method

The proposed method does not provide a favorable scaling with the number of parameters, which at present can be only up to $\rho = 3$. The main reason for this limitation is the adopted passivity characterization algorithm, which is based on a Cartesian adaptive sampling in a ρ-dimensional hypercube, and which requires a full SHH eigensolution at each computed parameter sample. The computing cost thus grows exponentially with ρ. All other components of the algorithm are less critical. For instance, high-dimensional Voronoi tessellation algorithms with reduced computational requirements are available [35]. Also the cost of model fitting through (3) with embedded constraints (10) scales only quadratically with the number of model coefficients rather than the dimension ρ of the embedding space. If scalability to a higher dimension is required, a new approach for passivity characterization would be required.

V. Examples

We present four numerical examples. The first two (Sec. V-A and V-B) are academic benchmarks intended for algorithm validation. The other two examples (an antenna in Sec. V-C and microwave filter in V-D) provide instead real application scenarios.

Algorithm 1 Algorithm for adaptive point selection

Require: Metric weights w', w'', w'''

Set number $\bar{q}_0$ of initial parameter points
Select $\bar{q}_0$ random parameter points
Evaluate system responses at $\mathcal{Q}_0 = \{\boldsymbol{\vartheta}_1, ..., \boldsymbol{\vartheta}_{\bar{q}_0}\}$
Build model $\mathbf{H}_0(s, \boldsymbol{\vartheta})$ as in (2), see Sec. II-A
Initialize refinement index $i = 1$
repeat
    Build Voronoi cells $C_{i;q}$, $q = 1, \ldots, \bar{q}_{i-1}$
    for each cell $C_{i;q}$ **do**
        Evaluate exploration metric $\Lambda'_{i,q}$ as in (11)
        Evaluate model error metric $\Lambda''_{i,q}$ as in (12)
        Evaluate passivity metric $\Lambda'''_{i,q}$ as in (19)
        Evaluate global metric $\Lambda_{i,q}$ as in (20)
    end for
    Select $\beta\,\bar{q}_{i-1}$ cells with highest $\Lambda_{i,q}$
    Add new points $\mathcal{P}_i$ in the selected cells
    Evaluate system responses at $\mathcal{P}_i$
    Build model $\mathbf{H}_i(s, \boldsymbol{\vartheta})$ on $\mathcal{Q}_i = \mathcal{Q}_{i-1} \cup \mathcal{P}_i$
    Evaluate worst-case model error $\mathcal{E}_i = \max_{q \in \mathcal{Q}_i} \mathcal{E}(\boldsymbol{\vartheta}_q)$
    Check passivity (Sec. II-B) and find $\Delta_{i,max}$ in (16)
    $i \leftarrow i + 1$
until $\mathcal{E}_i < \varepsilon$ and $\Delta_{i,max} < \varepsilon_p$
if model is not passive **then**
    Enforce model passivity, see Sec. II-D
end if
return Passive model $\widehat{\mathbf{H}}(s, \boldsymbol{\vartheta})$

A. A transmission-line network

We start by illustrating the behavior of proposed scheme using a transmission-line network. This example was initially used in [26] to illustrate the performance of the SHH passivity characterization and enforcement scheme, which is an important part of the adaptive sampling algorithm. The structure is composed of four cascaded segments of a lossy transmission line, with three internal loaded stubs. The choice of the free parameters is here different from [26]. We parameterize the internal line lengths, here denoted as $L \in [9, 10]$ mm, and the load terminating the central stub by means of its reflection coefficient $\Gamma \in [0.5, 0.9]$. The remaining line lengths are set to a fixed value of 7 mm, the stubs to 1 mm, while the reflection coefficients of the non-parameterized loads are set to 0.5. We seek for a macromodel reproducing frequency and parameter dependence of the scattering responses at the two terminal ports, from DC up to 20 GHz. The raw data ($\bar{k} = 500$ frequency samples for each parameter configuration) are obtained through an in-house Matlab script embedding both a quasi-static 2D field solver to determine the transmission-line parameters, and the frequency-domain solution of the distributed network.

The adaptive sampling loop is initialized with $\bar{q}_0 = 14$ points. After 5 iterations and a total of $\bar{q}_5 = 56$ available data points the algorithm stops, since model accuracy $\mathcal{E}(\boldsymbol{\vartheta})$ is uniformly below the prescribed threshold, here set to $\varepsilon = 10^{-3}$. This final model has $\bar{n} = 26$ poles, with a parameterization based on Chebychev polynomial bases of order

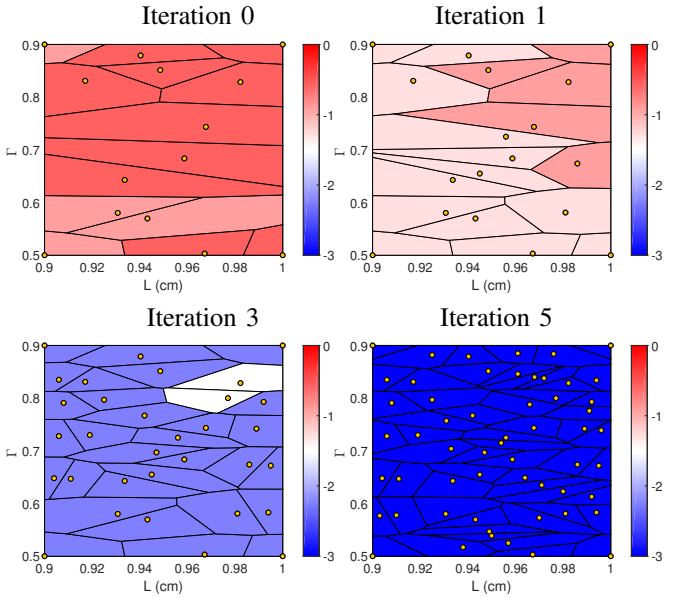


Fig. 5. TL-network example. The Voronoi tessellation of the parameter space at various adaptive sampling iterations is depicted, with the corresponding data points $\boldsymbol{\vartheta}_q$ (yellow circles). Each cell is colored according to the model-data error $\log_{10}(\mathcal{E}(\boldsymbol{\vartheta}_q))$ at the corresponding data point, confirming that the addition of new points at each new iteration lowers the error until all cells are characterized by a local error below the target threshold $\varepsilon = 10^{-3}$.

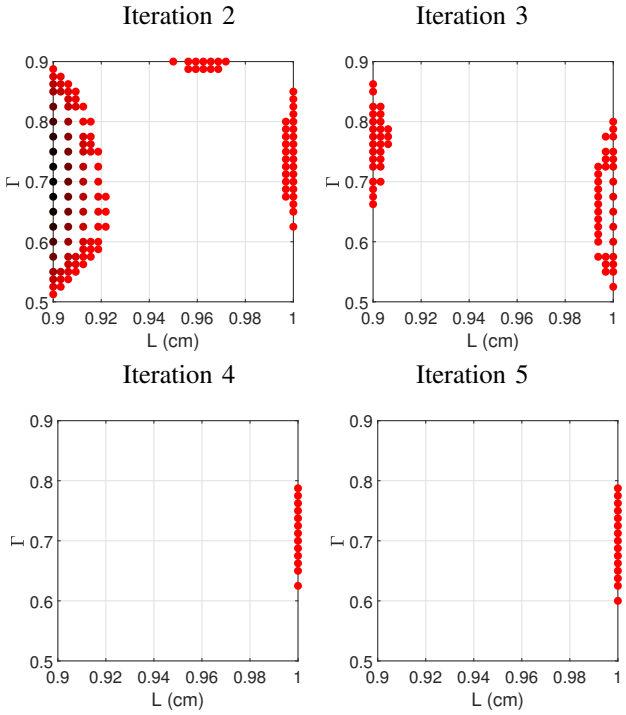


Fig. 6. TL network example. Evolution of points $\hat{\boldsymbol{\vartheta}}_p \in \mathcal{M}_i$ used to define the passivity-based metric. Dots are colored from red to black according to the passivity violation extent $\Delta_i(\hat{\boldsymbol{\vartheta}}_p) \in [0, \Delta_{\max}]$, where $\Delta_{\max} = \max_i \Delta_{i,\max} = 0.15$ is the worst-case passivity violation extent among all iterations (this normalization makes all panels comparable due to the common color scale).

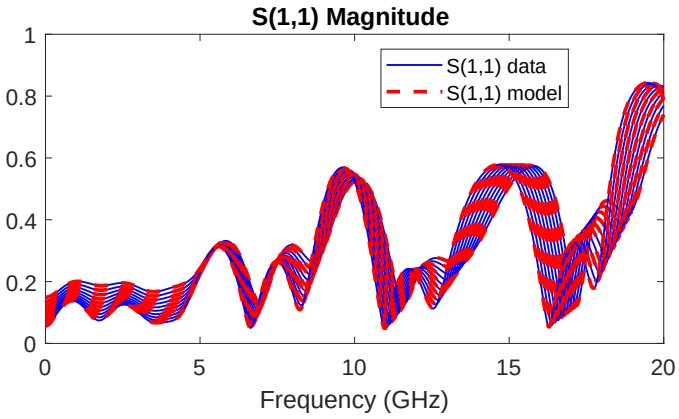


Fig. 7. TL network example. The plot reports ten frequency responses of the passive parameterized macromodel, evaluated over a linear sweep of both parameters L and Γ, i.e., along a diagonal of the rectangular parameter space. The model responses are compared to a set of validation responses evaluated for the true structure (not used for model identification).

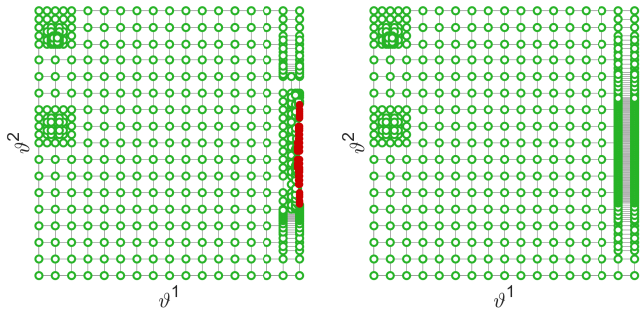


Fig. 8. Passivity characterization on final TL-network model before (left) and after (right) passivity enforcement. Empty green and filled red dots represent parameter configurations for which the model is passive or non-passive, respectively, within the ranges $\vartheta^1 = L \in [0.9, 1]$ cm and $\vartheta^2 = \Gamma \in [0.5, 0.9]$.

3 and 2, respectively, for the numerator and the denominator of (2). The evolution of the Voronoi cell distribution and the corresponding data points through iterations is depicted in Fig. 5, where the cells are colored using a color scale that is proportional to the error metric (4), so that visually the model is acceptable when all cells are colored in dark blue. Figure 6 depicts the location of the points $\hat{\boldsymbol{\vartheta}}_p \in \mathcal{M}_i$ corresponding to local (in-band) passivity violations at various iterations. The four panels confirm that the extent of the passivity violation is reduced through iterations, as the model becomes more and more accurate.

After the last iteration, the model presents some residual out-of-band passivity violations. Four iterations of the SHH passivity enforcement scheme are necessary to remove all passivity violations, obtaining a final uniformly passive model. A comparison between the frequency responses of the final passive model and the corresponding true responses generated just for validation (and not used for model identification) is reported in Fig. 7, confirming model accuracy. Figure 8 reports the location of the passivity violations in the parameter space before the final passivity enforcement, confirming that all violations are effectively removed.

A different parameterization is then considered for the same example, this time involving three parameters: the length of

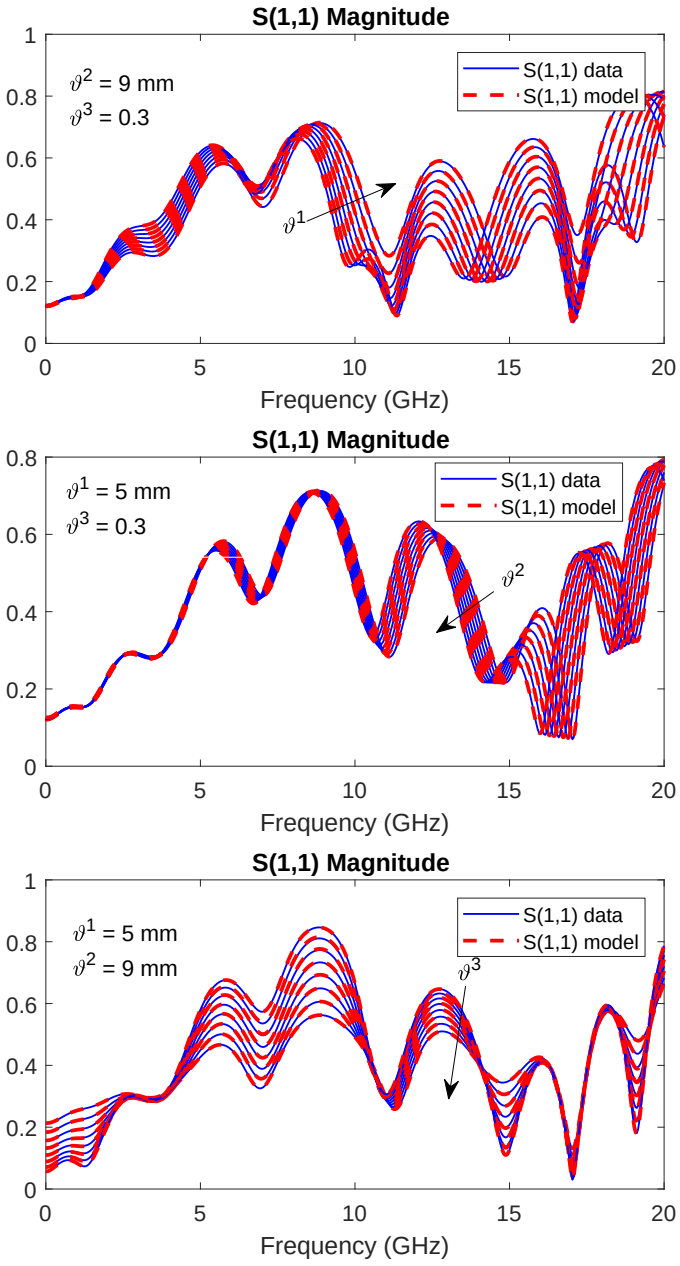


Fig. 9. Comparison between model responses and validation data of the TL-network for the 3D case. The three panels report eight frequency responses of the final passive model by sweeping only one parameter while freezing the other two (see legends). Top: $\vartheta^1 \in [5, 7]$ mm, $\vartheta^2 = 9$ mm, $\vartheta^3 = 0.3$; Middle: $\vartheta^1 = 5$ mm, $\vartheta^2 \in [9, 10]$ mm, $\vartheta^3 = 0.3$; Bottom: $\vartheta^1 = 5$ mm, $\vartheta^2 = 9$mm, $\vartheta^3 \in [0.3, 0.9]$.

the central stub $\vartheta^1 \in [5, 7]$ mm, the internal line lengths $\vartheta^2 \in [9, 10]$ mm, and the reflection coefficient of the central load $\vartheta^3 \in [0.3, 0.9]$. An accurate and passive model (28 poles with Chebychev polynomial orders $2, 3, 2$ for both numerator and denominator) is obtained after 5 iterations, for a total of $\bar{q}_5 = 56$ data points. The responses of the final model are reported in Fig. 9, whereas Fig. 10 confirms that the final model is passive throughout the parameter space.

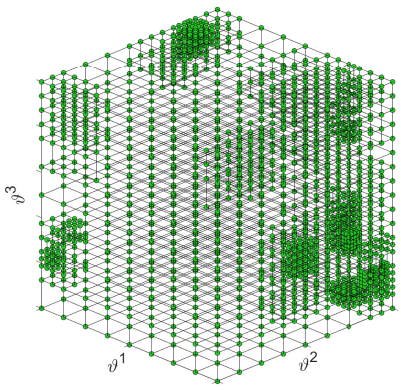


Fig. 10. Passivity characterization of the TL network model with three parameters, showing that no passivity violations are detected (see also Fig. 8).

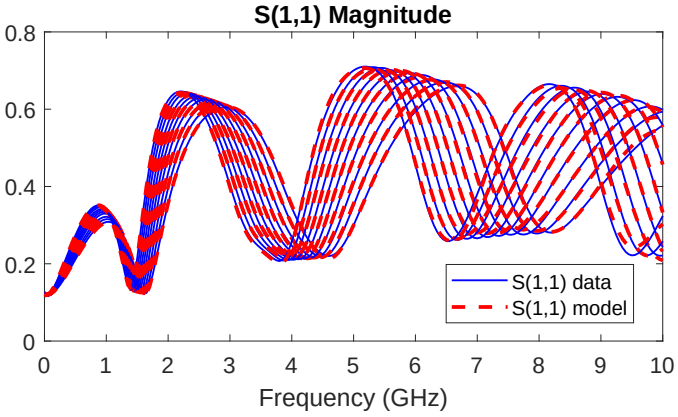


Fig. 11. PCB interconnect example. The plot reports ten frequency responses of the passive parameterized macromodel, evaluated over a linear sweep of both parameters along a diagonal of the rectangular parameter space. The model responses are compared to a set of validation responses evaluated for the true structure (not used for model identification).

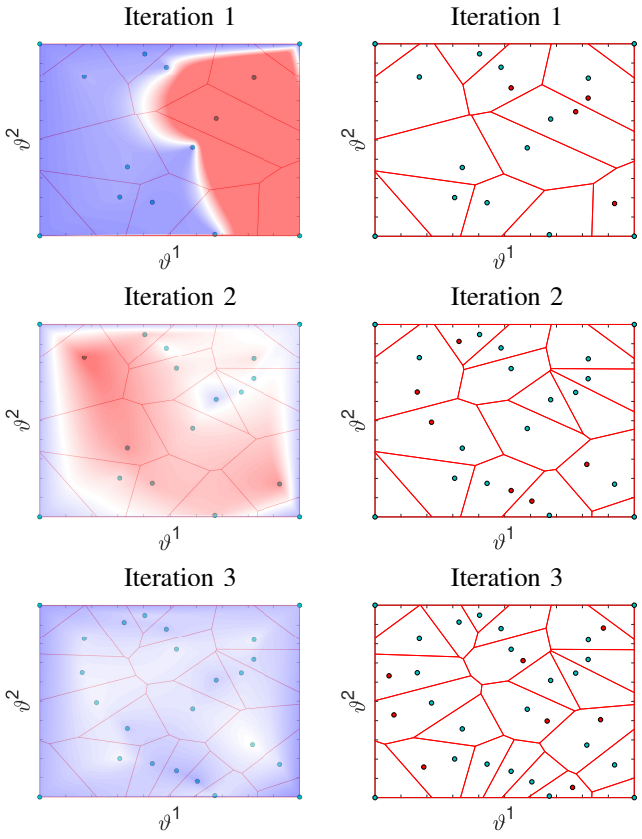


Fig. 12. PCB interconnect model. Left panels depict the parameter space subdivision into cells $C_{i;q}$ at iterations $i = 1, 2, 3$, together with the corresponding centers $\boldsymbol{\vartheta}_q$. The shades of color depict the global metric $\Lambda_{i;q}$ used for cell ranking and new sample selection (largest values are colored with red shades, smaller values with blue shades). Right panels show where the new samples are added for the next iteration (red dots).

B. A PCB interconnect with internal discontinuities

The second example we consider is a PCB interconnect with internal discontinuities composed by various coupled transmission line segments and lumped components, as depicted in Fig. 8 of [36]. With respect to [36], we modified the original circuit by changing each resistive termination with an electrical port with characteristic impedance $R_0 = 50\,\Omega$. The design parameters for this example are here defined to be the trace spacing ($\theta_1 \in [20, 40]\mu$m) and the length of the coupled lines sections ($\theta_2 \in [2.4, 3.0]$cm). We build a parameterized model for the reflection coefficient S_{11} at the input port of the interconnect from DC to 10 GHz. The raw frequency responses used to construct the model are obtained by linking the adaptive sampling loop to SPICE, which solves on-demand the transmission-line network for the new points to be added at each iteration. Each frequency sweep uses $\bar{k} = 201$ samples.

The proposed adaptive sampling loop is initialized also in this case with $\bar{q}_0 = 14$ starting samples and stops after 4 iterations with $\bar{q}_4 = 42$ points, obtaining a model with $\bar{n} = 20$ poles and Chebychev polynomial bases of order $\bar{\ell}_1 = \bar{\ell}_2 = 2$ for both numerator and denominator in (2). Figure 11 compares the frequency responses of the final passive macromodel obtained as a result of proposed adaptive sampling loop to the true responses of the structure. As for the TL network example, the validation responses of Fig. 11 are computed ad hoc just for validation and do not belong to the automatically-determined set of responses used for model identification. The plot confirms the uniform good accuracy of the model throughout the sweep, demonstrating the excellent interpolation/approximation capability of the proposed modeling framework.

Figure 12 provides some insight on the adaptive sampling process. The left panels show through an interpolated color shade the values of the global metric used to rank the cells and flag those that need refinement. Red (blue) shades correspond to the largest (smallest) values of the metric. The right panels show where new points are added at each iteration (red dots). We see that, as iterations progress, the global metric values become smaller and more uniform. This is expected, since when the overall set of grid points is adequate for model generation, the criteria for mesh refinement are supposed to be not compelling as in the first iterations, where refinement is needed.

C. H-shaped antenna

The third example we consider is a microwave H-antenna presented and described in full detail in [20]. The frequency band of interest varies between f_{min} = 4.5 GHz and f_{max} = 5.5 GHz. Both the length L of the antenna and width W of the aperture are parameterized, respectively, within the ranges $L \in [6, 7.1]$ mm and $W \in [1.01, 1.1]$ mm. The proposed adaptive sampling scheme has been linked with the EM simulator ADS-Momentum, which is used to extract the frequency response (a total of $\bar{k} = 100$ frequency samples for each parameter configuration) of the antenna at the feeding port.

The adaptive algorithm for the selection of new simulation points performs 5 iterations before reaching an overall model accuracy of 10^{-3}. The result of each iteration of the algorithm is reported in Fig. 13, where the Voronoi tessellation of the design space is depicted, together with a color metric indicating the error, in logarithmic scale, of the intermediate macromodels built with the current set of points. The four panels of Fig. 13 show that the model accuracy over the parameter space increases progressively after each iteration, until a final model with $\bar{n} = 12$ poles and polynomial orders 3 and 1 for numerator and denominator of (2), respectively, is obtained.

It is worth noticing that the same example required 225 simulation points over the parameter space using the algorithm of [20], whereas proposed scheme terminates with only $\bar{q}_5 = 56$ points. Figure 14 compares the model responses to a set of validation data samples computed by sweeping 10 points along the diagonal of the parameter space (these points not used for model construction). As for the other examples, no visual difference can be noted between parameterized model responses and validation data.

We now provide some details on runtime (measured using a Core-i7-based laptop running at 2.8 GHz with 16 GB RAM). For this test case the field simulation of a single parameter configuration requires about 148 s for a frequency sweep over the band of interest. At the end of the adaptive sampling loop, the cumulative time required by the field solver amounts to 2.3 hours (excluding the validation data samples, which are not used for model construction). The cumulative runtime required by point selection, construction of intermediate macromodels (five, one for each iteration), SHH passivity characterization, construction and evaluation of the global metric, is about 216 s. Therefore, only 2.5% of the overall runtime is spent by the various components of proposed algorithm, while the remaining 97.5% is due to the field solver. These results confirm the suitability of a model-driven approach for model construction, since the computational requirements of the macromodeling part are negligible.

D. Coupled line bandpass filter

The last example is a coupled line microstrip bandpass filter. Figure 15 shows a top view of the structure, which consists of a PEC cover, an Alumina layer with 0.635 mm thickness ($\varepsilon_r = 9.9$, $\tan\delta = 0.0009$) and a Gold layer with 0.178 mm thickness. The frequency band of interest

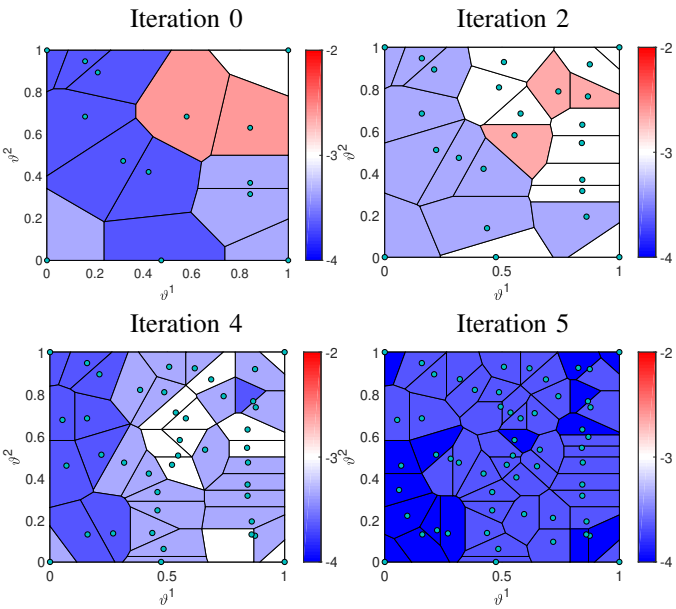


Fig. 13. As in Fig. 5, but for the H-antenna example. The color scale used for each cell represents the corresponding local model-data error $\log_{10}(\mathcal{E}(\boldsymbol{\vartheta}_q))$.

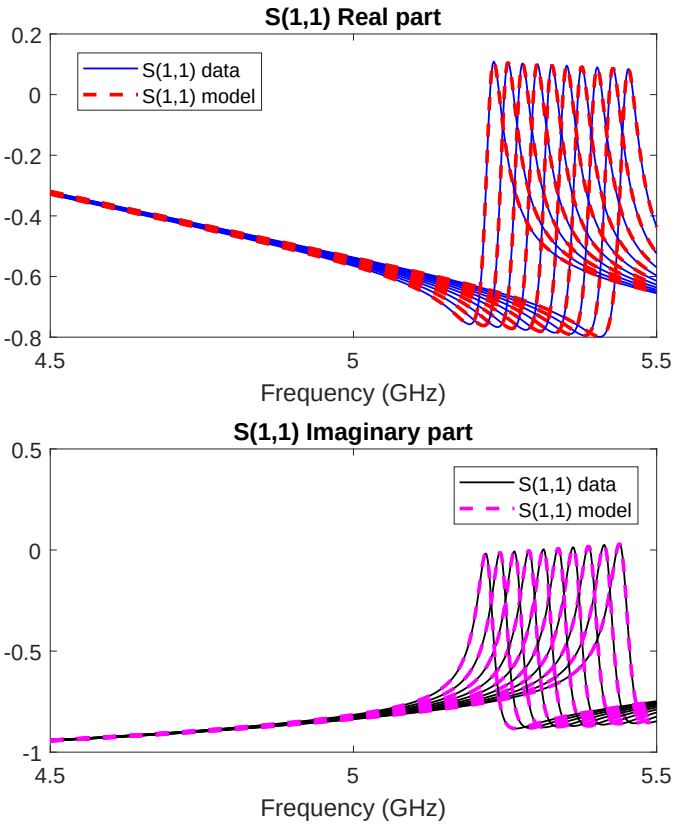


Fig. 14. Comparison between passive model responses and validation data of the H-antenna.

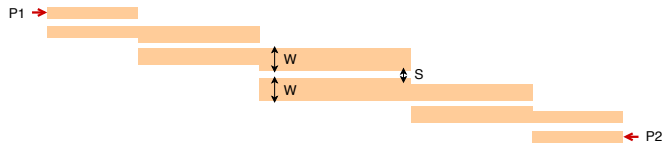


Fig. 15. A top-view of the coupled line microstrip bandpass filter.

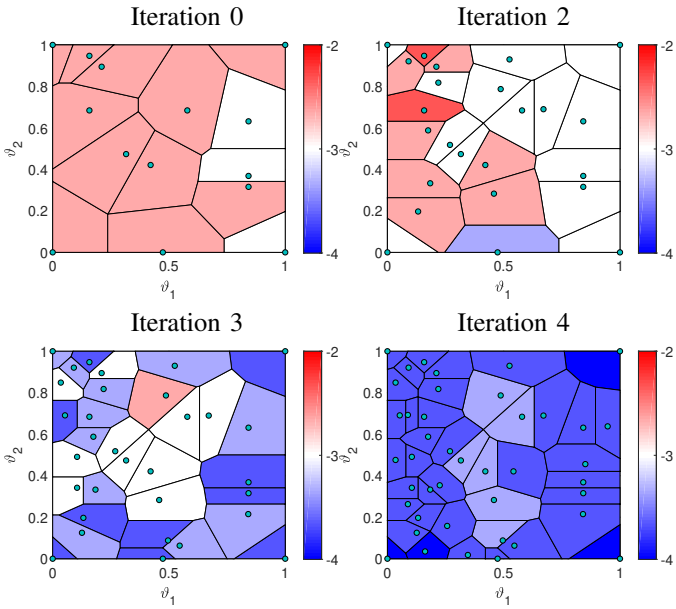


Fig. 16. As in Fig. 5, but for the coupled line filter example. The color scale used for each cell represents the corresponding local model-data error $\log_{10}(\mathcal{E}(\boldsymbol{\vartheta}_q))$.

ranges from $f_{min} = 1$ GHz to $f_{max} = 7$ GHz. The parameters are the width $W \in [0.635, 0.889]$ mm and the spacing $S \in [0.635, 0.889]$ mm, as reported in Figure 15. The system responses are retrieved from the EM simulator ADS-Momentum ($\bar{k} = 300$ frequency samples for each parameter configuration). For this example 4 iterations of the algorithm are necessary to obtain an overall accuracy below the threshold of 10^{-3}, for a total of 42 points in the parameter space. The final model has $\bar{n} = 20$ poles and Chebychev polynomial bases of order $\bar{\ell}_1 = \bar{\ell}_2 = 5$ for the numerator and $\bar{\ell}_1 = \bar{\ell}_2 = 4$ for the denominator. The Voronoi diagrams of the parameter space for successive iterations of the algorithm are reported in Figure 16, and they clearly show the gradual improvement in model accuracy over successive iterations of the algorithm. Finally, Fig. 17 compares ten model responses to ten validation responses evaluated from the real structure over a linear sweep across the diagonal of the parameter space (not used for model identification). For what concerns the runtime, the algorithm devoted to the adaptive selection of new points by means of the three metrics and intermediate model identification (four, one for each iteration) takes a cumulative time of 417 s. The total runtime required by EM solver for simulation of the 42 fitting responses used for model construction amounts to 1.2 hours. This means that less than 9% of the total time required for model construction in spent by the proposed algorithm, while the rest is employed by the EM solver.

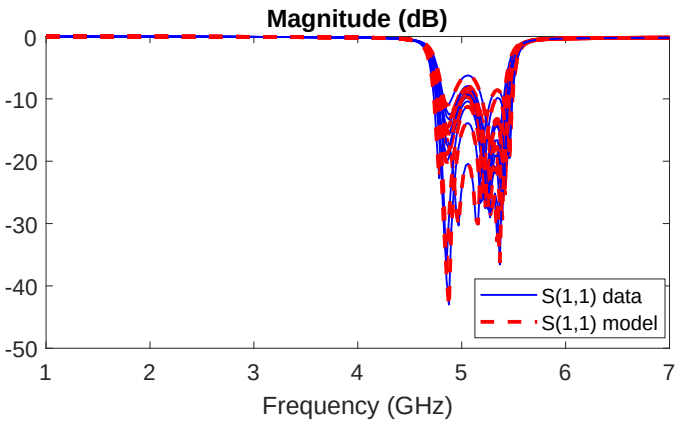


Fig. 17. Model responses for coupled line filter example.

VI. Conclusions

This paper presented a novel adaptive sampling scheme for the automated determination of a minimal set of data samples to be used for the construction of a parameterized macromodel. The proposed method belongs to the class of model-based approaches, which drive the adaptive sampling process using the information provided by intermediate surrogate models constructed at each pass of the adaptive sampling loop. The main novel contribution of this work is a passivity-based metric, which identifies the regions of the parameter space where the intermediate models are not passive hence not physically-consistent. The extent of the local passivity violations is used as a quantitative criterion to increase sampling density in their neighborhood, thus helping the overall macromodeling scheme in improving accuracy uniformly in the parameter space.

The proposed scheme provides good results for the cases that were tested. It should be emphasized that this approach, as all closed-form parameterization schemes available in the literature, is appropriate only for a limited number of free parameters, in this work up to $\rho = 3$. A higher dimension in the parameter space will be difficult to handle in case all parameters are uncorrelated and exhibit significant variations to be captured by a proper model parameterization. Work is under way to extend the maximum dimension of the parameter space, and especially to investigate the limits within which the present approach can be meaningfully applied.

References

[1] M. Swaminathan, D. Chung, S. Grivet-Talocia, K. Bharath, V. Laddha, and J. Xie, "Designing and modeling for power integrity," *IEEE Transactions on Electromagnetic Compatibility*, vol. 52, no. 2, pp. 288–310, May 2010.

[2] R. Achar and M. S. Nakhla, "Simulation of high-speed interconnects," *Proceedings of the IEEE*, vol. 89, no. 5, pp. 693–728, May 2001.

[3] P. Benner, M. Hinze, and E. J. W. ter Maten, *Model reduction for circuit simulation*. Springer, 2010, vol. 74.

[4] T. Reis. Circuit synthesis of passive descriptor systems: a modified nodal approach. *International Journal of Circuit Theory and Applications*, 38(1):44–68, 2010.

[5] T. Kailath. *Linear systems*. Prentice-Hall Englewood Cliffs, NJ, 1980.

[6] B. D. O. Anderson and S. Vongpanitlerd, *Network analysis and synthesis*. Prentice-Hall, 1973.

[7] S. Grivet-Talocia and B. Gustavsen, *Passive macromodeling: Theory and applications*. John Wiley & Sons, 2015, vol. 239.

[8] B. Gustavsen and A. Semlyen, "Rational approximation of frequency domain responses by vector fitting," *Power Delivery, IEEE Transactions on*, vol. 14, no. 3, pp. 1052–1061, jul 1999.

[9] A. J. Mayo and A. C. Antoulas, "A framework for the solution of the generalized realization problem," *Linear algebra and its applications*, vol. 425, no. 2-3, pp. 634–662, 2007.

[10] S. Lefteriu and A. C. Antoulas, "A new approach to modeling multiport systems from frequency-domain data," *Computer-Aided Design of Integrated Circuits and Systems, IEEE Transactions on*, vol. 29, no. 1, pp. 14–27, jan. 2010.

[11] P. Triverio, S. Grivet-Talocia, and M. S. Nakhla, "A parameterized macromodeling strategy with uniform stability test," *IEEE Trans. Advanced Packaging*, vol. 32, no. 1, pp. 205–215, Feb 2009.

[12] S. Grivet-Talocia and E. Fevola, "Compact parameterized black-box modeling via fourier-rational approximations," *IEEE Transactions on Electromagnetic Compatibility*, vol. 59, no. 4, pp. 1133–1142, 2017.

[13] A. Ionita and A. Antoulas, "Data-driven parametrized model reduction in the loewner framework," *SIAM Journal on Scientific Computing*, vol. 36, no. 3, pp. A984–A1007, 2014.

[14] F. Ferranti, L. Knockaert, and T. Dhaene, "Parameterized s-parameter based macromodeling with guaranteed passivity," *IEEE Microwave and Wireless Components Letters*, vol. 19, no. 10, pp. 608–610, 2009.

[15] F. Ferranti, L. Knockaert, T. Dhaene, and G. Antonini, "Passivity-preserving parametric macromodeling for highly dynamic tabulated data based on lur'e equations," *IEEE Transactions on Microwave Theory and Techniques*, vol. 58, no. 12, pp. 3688–3696, 2010.

[16] F. Ferranti, L. Knockaert, and T. Dhaene, "Passivity-preserving parametric macromodeling by means of scaled and shifted state-space systems," *IEEE Transactions on Microwave Theory and Techniques*, vol. 59, no. 10, pp. 2394–2403, 2011.

[17] F. Ferranti, T. Dhaene, and L. Knockaert, "Compact and passive parametric macromodeling using reference macromodels and positive interpolation operators," *Components, Packaging and Manufacturing Technology, IEEE Transactions on*, vol. 2, no. 12, pp. 2080–2088, Dec 2012.

[18] E. R. Samuel, L. Knockaert, F. Ferranti, and T. Dhaene, "Guaranteed passive parameterized macromodeling by using sylvester state-space realizations," *IEEE Transactions on Microwave Theory and Techniques*, vol. 61, no. 4, pp. 1444–1454, 2013.

[19] S. Koziel and A. T. Sigurösson, "Triangulation-Based Constrained Surrogate Modeling of Antennas," in IEEE Transactions on Antennas and Propagation, vol. 66, no. 8, pp. 4170-4179, Aug. 2018.

[20] D. Deschrijver, K. Crombecq, H. M. Nguyen and T. Dhaene, "Adaptive Sampling Algorithm for Macromodeling of Parameterized S-Parameter Responses," *IEEE Transactions on Microwave Theory and Techniques*, vol. 59, no. 1, pp. 39–45, 2011.

[21] A. Lamecki, P. Kozakowski, M. Mrozowski, "Efficient implementation of the Cauchy method for automated CAD-model construction", IEEE Microw. Wireless Compon. Lett., vol. 13, no. 7, pp. 268-270, Jul. 2003.

[22] R. Lehmensiek, P. Meyer, "Creating accurate multivariate rational interpolation models for microwave circuits by using efficient adaptive sampling to minimize the number of computational electromagnetic analyses", IEEE Trans. Microw. Theory Tech., vol. 49, no. 8, pp. 1419-1419, Aug. 2001.

[23] S. F. Peik, R. R. Mansour, and Y. L. Chow, "Multidimensional Cauchy method and adaptive sampling for an accurate microwave circuit modeling," IEEE Trans. Microwave Theory Tech., vol. 46, pp. 2364–2371, Dec. 1998

[24] G. Antonini, D. Deschrijver, and T. Dhaene. Broadband rational macromodeling based on the adaptive frequency sampling algorithm and the partial element equivalent circuit method. *Electromagnetic Compatibility, IEEE Transactions on*, 50(1):128–137, 2008.

[25] A. Zanco, S. Grivet-Talocia, T. Bradde and M. De Stefano, "Multivariate macromodeling with stability and passivity constraints," 2018 IEEE 22nd Workshop on Signal and Power Integrity (SPI), Brest, 2018, pp. 1-4.

[26] A. Zanco, S. Grivet-Talocia, T. Bradde, and M. De Stefano, "Enforcing passivity of parameterized LTI macromodels via Hamiltonian-driven multivariate adaptive sampling," IEEE Transactions on Computer-Aided Design of Integrated Circuits and Systems, 2019; in press.

[27] S. Grivet-Talocia, "A perturbation scheme for passivity verification and enforcement of parameterized macromodels," *IEEE Transactions on Components, Packaging and Manufacturing Technology*, vol. 7, no. 11, pp. 1869–1881, 2017.

[28] S. Grivet-Talocia and R. Trinchero, "Behavioral, parameterized, and broadband modeling of wired interconnects with internal discontinuities," *IEEE Transactions on Electromagnetic Compatibility*, vol. 60, no. 1, pp. 77–85, 2018.

[29] E. Fevola, A. Zanco, S. Grivet-Talocia, T. Bradde, M. De Stefano "An Adaptive Algorithm for Fully Automated Extraction of Passive Parameterized Macromodels", submitted to the *2019 IEEE MTT-S International Conference on Numerical Electromagnetic and Multiphysics Modeling and Optimization, May 29-31, 2019, Cambridge, MA, USA.*

[30] D. Deschrijver, T. Dhaene, D. De Zutter, "Robust parametric macromodeling using multivariate orthonormal vector fittin", IEEE Trans. Microw. Theory Tech., vol. 56, no. 7, pp. 1661-1667, Jul. 2008

[31] C. Sanathanan and J. Koerner, "Transfer function synthesis as a ratio of two complex polynomials," *Automatic Control, IEEE Transactions on*, vol. 8, no. 1, pp. 56–58, jan 1963.

[32] M. R. Wohlers, *Lumped and Distributed Passive Networks*. Academic press, 1969.

[33] S. P. Boyd and L. Vandenberghe, *Convex optimization*. Cambridge University Press, 2004.

[34] F. Aurenhammer, "Voronoi diagrams–a survey of a fundamental geometric data structure", ACM Comput. Surveys, vol. 23, no. 3, pp. 345-405, 1991.

[35] Dwyer, Rex A, "Higher-dimensional Voronoi diagrams in linear expected time", Discrete & Computational Geometry, vol. 6, no. 3, pp. 343–367, 1991, Springer.

[36] P. Manfredi, D. Vande Ginste, D. De Zutter and F. G. Canavero, "Uncertainty Assessment of Lossy and Dispersive Lines in SPICE-Type Environments", IEEE Transactions on Components, Packaging and Manufacturing Technology, Vol. 3, No. 7, pp. 1252–1258, July 2013.

[37] J. H. Wilkinson, *The algebraic eigenvalue problem*. Clarendon Press, 1965.

[38] P. Benner, D. Kressner, and V. Mehrmann. Skew-Hamiltonian and Hamiltonian eigenvalue problems: Theory, algorithms and applications. In Z. Drmac, M. Marusic, and Z. Tutek, editors, *Proceedings of the Conference on Applied Mathematics and Scientific Computing*, pages 3–39. Springer Netherlands, 2005.

[39] V. Mehrmann and D. Watkins. Structure-preserving methods for computing eigenpairs of large sparse skew-Hamiltonian/Hamiltonian pencils. *SIAM Journal on Scientific Computing*, 22(6):1905–1925, 2001.

[40] R. Alam, S. Bora, M. Karow, V. Mehrmann, and J. Moro. Perturbation theory for Hamiltonian matrices and the distance to bounded-realness. *SIAM J. Matrix Analysis Applications*, 32(2):484–514, 2011.



Elisa Fevola received the Bachelor degree in Electronic Engineering in 2016 and the Master degree in Electronic Engineering in 2018 from Politecnico di Torino, Turin, Italy. She also received the M.Sc. in Electrical and Computer Engineering in 2018 from the University of Illinois at Chicago, Chicago, USA. She is currently pursuing her Ph.D. in Electrical, Electronics and Communications Engineering at Politecnico di Torino. Her current research interests include parameterized macromodeling and model order reduction for multi-physics systems, with an emphasis on cardiovascular applications.



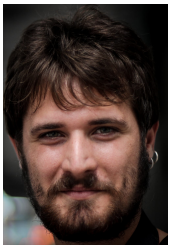
Alessandro Zanco received the Bachelor Degree in Electrical Engineering in 2015 and the Master degree in Mechathronic Engineering in 2018 from Politecnico di Torino, Turin, Italy. He is currently pursuing his Ph.D in Electrical, Electronics and Communications Engineering, at Politecnico di Torino. His research interests include high-dimensional parametric black-box modeling for EMC, with emphasis on sparse model representations and passivity verification techniques. He is co-recipient of the 2018 Best Paper Award of the IEEE INTERNATIONAL SYMPOSIUM ON ELECTROMAGNETIC COMPATIBILITY.



Stefano Grivet-Talocia (M'98–SM'07–F'18) received the Laurea and Ph.D. degrees in electronic engineering from the Politecnico di Torino, Turin, Italy.

From 1994 to 1996, he was with the NASA/Goddard Space Flight Center, Greenbelt, MD, USA. He is currently a Full Professor of electrical engineering with the Politecnico di Torino. He co-founded the academic spinoff company IdemWorks in 2007, serving as the President until its acquisition by CST in 2016. He has authored over 150 journal and conference papers. His current research interests include passive macromodeling of lumped and distributed interconnect structures, model-order reduction, modeling and simulation of fields, circuits, and their interaction, wavelets, time-frequency transforms, and their applications.

Dr. Grivet-Talocia was a co-recipient of the 2007 Best Paper Award of the IEEE TRANSACTIONS ON ADVANCED PACKAGING. He received the IBM Shared University Research Award in 2007, 2008, and 2009. He was an Associate Editor of the IEEE TRANSACTIONS ON ELECTROMAGNETIC COMPATIBILITY from 1999 to 2001 and He is currently serving as Associate Editor for the IEEE TRANSACTIONS ON COMPONENTS, PACKAGING AND MANUFACTURING TECHNOLOGY. He was the General Chair of the 20th and 21st IEEE Workshops on Signal and Power Integrity (SPI2016 and SPI2017).



Tommaso Bradde received the Bachelor degree in Electronic Engineering from the Università degli studi Roma Tre, Rome, Italy, in 2015 and the master degree in Mechatronic Engineering at Politecnico di Torino, Turin, Italy, in 2018. He is currently a first-year Ph.D. student in Electrical, Electronics and Communications Engineering within the Politecnico di Torino. His current research is focused on data-driven parameterized macromodeling and its applications to system level power integrity assessments which include active devices.

He is co-recipient of the 2018 Best Paper Award of the IEEE INTERNATIONAL SYMPOSIUM ON ELECTROMAGNETIC COMPATIBILITY.



Marco De Stefano received the M.Sc. degree in mechatronic engineering from Politecnico di Torino, Turin, Italy, in 2018. He is currently pursuing his Ph.D. in Electrical, Electronics and Communications Engineering at the Politecnico di Torino. His current research interests include model-order reduction, with emphasis on parameterized macromodeling, compressed macromodeling via data compression techniques, topological modeling and fast simulation methods for signal and power integrity. He is co-recipient of the 2018 Best Paper Award of the IEEE INTERNATIONAL SYMPOSIUM ON ELECTROMAGNETIC COMPATIBILITY.